

The Molecular Exoskeleton of the Ring-like Planetary Nebula NGC 3132

JOEL H. KASTNER,^{1,2,3} DAVID J. WILNER,⁴ PAULA MORAGA BAEZ,^{2,3} JESSE BUBLITZ,⁵ ORSOLA DE MARCO,^{6,7}
RAGHVENDRA SAHAI,⁸ AND AL WOOTTEN⁹

¹*Center for Imaging Science, Rochester Institute of Technology, Rochester NY 14623, USA; jhk@cis.rit.edu*

²*School of Physics and Astronomy, Rochester Institute of Technology*

³*Laboratory for Multiwavelength Astrophysics, Rochester Institute of Technology*

⁴*Center for Astrophysics, Harvard & Smithsonian, 60 Garden Street, Cambridge, MA 02138-1516, USA*

⁵*Green Bank Observatory, 155 Observatory Road, Green Bank, WV 24944, USA; jbublitz@nrao.edu*

⁶*School of Mathematical and Physical Sciences, Macquarie University, Sydney, New South Wales, Australia*

⁷*Astronomy, Astrophysics and Astrophotonics Research Centre, Macquarie University, Sydney, New South Wales, Australia*

⁸*Jet Propulsion Laboratory, California Institute of Technology, 4800 Oak Grove Drive, Pasadena, CA 91109, USA*

⁹*National Radio Astronomy Observatory, Charlottesville, VA 22903, USA*

ABSTRACT

We present Submillimeter Array (SMA) mapping of $^{12}\text{CO } J = 2 \rightarrow 1$, $^{13}\text{CO } J = 2 \rightarrow 1$, and CN $N = 2 \rightarrow 1$ emission from the Ring-like planetary nebula (PN) NGC 3132, one of the subjects of JWST Early Release Observation (ERO) near-infrared imaging. The $\sim 5''$ resolution SMA data demonstrate that the Southern Ring's main, bright, molecule-rich ring is indeed an expanding ring, as opposed to a limb-brightened shell, in terms of its intrinsic (physical) structure. This suggests that NGC 3132 is a bipolar nebula viewed more or less pole-on (inclination $\sim 15\text{--}30^\circ$). The SMA data furthermore reveal that the nebula harbors a second expanding molecular ring that is aligned almost orthogonally to the main, bright molecular ring. We propose that this two-ring structure is the remnant of an ellipsoidal molecular envelope of ejecta that terminated the progenitor star's asymptotic giant branch evolution and was subsequently disrupted by a series of misaligned fast, collimated outflows or jets resulting from interactions between the progenitor and one or more companions.

1. INTRODUCTION

Planetary nebulae (PNe) are the near-endpoints of stellar evolution for intermediate-mass ($\sim 1\text{--}8 M_\odot$) stars. Each PN provides a snapshot of the brief ($\sim 10^4$ yr) stage in which the outflowing, dusty circumstellar envelope of an asymptotic giant branch (AGB) star is ionized by its newly unveiled core, itself a future white dwarf. The resulting $\sim 10^4$ K circumstellar plasma is a rich source of optical emission lines, forming a classical PN. However, certain PNe retain cold (< 100 K), dense ($\sim 10^4\text{--}10^6 \text{ cm}^{-3}$), massive envelopes of molecular gas and dust. These PN molecular envelopes are shaped and displaced by fast winds from their exceedingly hot ($\sim 100\text{--}200$ kK), rapidly evolving central stars, which are also sources of intense UV irradiation of the molecular gas.

The molecule-rich zones of PNe have been detected via IR imaging of H₂ rovibrational emission, which reveals shock-heated and/or UV-irradiated molecular gas (e.g., Webster et al. 1988; Zuckerman & Gatley 1988; Kastner et al. 1994, 1996), and by mm-wave spectroscopy of CO rotational emission from far colder and more massive molecular reservoirs within PNe (e.g., Huggins et al. 1996, 2005). The vast majority of such molecule-rich PNe, most of which are detected in both near-IR H₂ and mm-wave CO, are Ring-like or bipolar in structure; these objects likely constitute a PN class descended from relatively massive progenitor stars (Kastner et al. 1996, and references therein). Interferometric observations of such molecule-rich planetary nebulae in the mm-wave regime afford unparalleled opportunities to study their density structures, kinematics, and compositions. The resulting high-resolution molecular line maps of PNe can provide — among other things — stringent tests of models of the shaping of such nebulae by collimated outflows from central binary systems as well as insight into the enrichment of the ISM in the products of intermediate-mass stellar nucleosynthesis (e.g., Kastner et al. 2018).

Here, we present Submillimeter Array (SMA) mapping of molecular emission from the PN NGC 3132. NGC 3132 is a nearby ($D = 754$ pc), “Ring-like” PN that harbors a wide visual binary comprising the central (progenitor) star and an A star companion (Ciardullo et al. 1999). The inner, ionized cavity of NGC 3132 is elliptical in shape, with a major axis of ~ 40 arcsec (0.15 pc) and an electron density of $n \sim 10^3$ cm $^{-3}$. The PN’s ionization structure and abundances were the subject of a recent optical (VLT/MUSE) spectroscopic mapping study (Monreal-Ibero & Walsh 2020).

Like other PNe in its (Ring-like) class (Kastner et al. 1994), NGC 3132 has long been known to harbor a significant mass of molecular gas, as revealed by H $_2$ and CO emission (Storey 1984; Sahai et al. 1990; Zuckerman et al. 1990; Kastner et al. 1996). JWST Early Release Observation (ERO) imaging of NGC 3132 has now revealed the structure of its H $_2$ emission region in unprecedented detail (De Marco et al. 2022). The JWST H $_2$ images reveal a complex ring system surrounding the central ionized region, as well as a system of arcs within the nebula’s extended halo. De Marco et al. (2022) assert that these structures were most likely sculpted by an unseen companion or companions orbiting within ~ 60 au of the PN progenitor. Furthermore, the mid-IR JWST (MIRI) images demonstrate the ultra-hot central star has a significant IR excess that most likely emanates from a dusty disk that formed as the result of a close binary interaction, albeit not necessarily with the same companion that generated the H $_2$ ring and arc systems (De Marco et al. 2022; Sahai et al. 2023).

The H $_2$ emission imaged by JWST only traces the hot (~ 1000 K), UV-illuminated and/or shock-excited molecular gas in the nebula, and such hot H $_2$ likely constitutes a small fraction of the total reservoir of molecular gas in NGC 3132. Furthermore, JWST imaging does not provide any information concerning the molecular gas kinematics, such as can be obtained via mm-wave molecular line mapping. However, the only previous such molecular line mapping of NGC 3132 consists of a single-dish ^{12}CO map obtained with the late SEST facility (beamwidth $\sim 20''$) well over 30 yr ago (Sahai et al. 1990). These SEST observations revealed strong CO emission from the PN’s central ring system that is characterized by expansion at ~ 15 km s $^{-1}$, with hints of faster (> 20 km s $^{-1}$) outflows. The only other molecule that has been detected in NGC 3132 thus far (apart from CO and H $_2$) is HCO $^+$ (Sahai et al. 1993).

To establish the distribution, mass, and velocity structure of the molecular gas in NGC 3132, and to probe its molecular gas composition, we have used the SMA to map the nebula in $^{12}\text{CO}(2-1)$, as well as the 2–1 rotational transitions of CN and CO isotopologues. In this paper, we present the SMA observations of NGC 3132, and describe how these observations yield new insight into the PN’s three-dimensional structure and molecular chemistry.

2. OBSERVATIONS

We observed NGC 3132 with the Submillimeter Array (SMA) on 2023 May 16. The six operating antennas were in a compact configuration that provided baseline lengths from 6 to 68 meters. NGC 3132 is a challenging target for the SMA due to its southern declination (-40°) and consequent low elevations when observed from Maunakea, requiring favorable weather conditions. For these observations, the 225 GHz atmospheric opacity was 0.06 with very stable phase throughout. The two dual-sideband receivers were tuned to LO frequencies of 225.538 and 235.538 GHz. With each receiver providing an IF range of 4-16 GHz, this setup provided continuous spectral coverage from 209.5 to 251.5 GHz. The SWARM digital backend provided 140 kHz channel spacing over the full bandwidth, which corresponds to 0.18 km s $^{-1}$ at the frequency of the $^{12}\text{CO } J = 2 \rightarrow 1$ line (230.538 GHz). The SMA primary beam size is $55''$ (FWHM) at this frequency. With baselines down to 6 meters, these SMA observations have a maximum recoverable scale of $\sim 27''$.

We observed NGC 3132 in a small hexagonal mosaic of 7 pointings with $30''$ spacing to span the full extent of $^{12}\text{CO } J = 2 \rightarrow 1$ emission previously imaged with the SEST telescope (Sahai et al. 1990). The observing sequence consisted of 2 minutes on each of the 7 mosaic pointings, bracketed by the two calibrators J1037-295 and J1001-446. The target was observed over the hour angle range -2.1 to 2.8 .

We used the MIR software package to calibrate the visibilities following standard procedures for SMA data. The visibilities were initially inspected manually to flag a small number of channels that showed evidence for interference. The bandpass response was determined from observations of the strong source 3C 279, the absolute flux scale was set from a short observation of the asteroid Ceres (with $\sim 10\%$ estimated systematic uncertainty), and time dependent complex gains were derived and applied from observations of J1037–295 (the stronger of the two gain calibrators, 1.31 Jy).

We used the MIRIAD software package to make images, using the mosaic option in the `invert` task followed by clean deconvolution with the `mosstdi` task. We imaged the $^{12}\text{CO } J = 2 \rightarrow 1$, $^{13}\text{CO } J = 2 \rightarrow 1$, $\text{C}^{18}\text{O } J = 2 \rightarrow 1$, and CN $N = 2 \rightarrow 1$ (226.875 GHz hyperfine complex) lines by generating image cubes over velocity bins of 1.5 km s $^{-1}$ width, chosen as a compromise between resolving kinematic structure and signal-to-noise ratio. Table 1 lists the transition

Table 1. SMA MOLECULAR EMISSION LINE OBSERVATIONS OF NGC 3132

Molecule (Trans.)	ν (GHz)	beam size (arcsec ²)	beam PA	rms (mJy beam ⁻¹)	I^a (Jy km s ⁻¹)
¹² CO ($J = 2 \rightarrow 1$)	230.538000	6.5×2.5	-12°	130	1710±6
¹³ CO ($J = 2 \rightarrow 1$)	220.398684	6.7×2.6	-11°	101	36±9
C ¹⁸ O ($J = 2 \rightarrow 1$)	219.560354	6.9×2.7	-8°	102	<27
CN ($N = 2 \rightarrow 1$)	226.874781 ^b	6.4×2.6	-10°	117	199±9
continuum	228.7	6.8×2.7	-8°	4.2	... ^c

NOTES:

- a) Integrated intensity of emission and associated statistical uncertainty; estimated systematic flux uncertainties are $\sim 10\%$ (see text).
b) Frequency of brightest component of hyperfine complex.
c) 3σ upper limit on 228.7 GHz continuum flux is ~ 12 mJy beam⁻¹.

frequency, beam size and position angle (PA) as obtained with robust=0 weighting, rms channel-to-channel noise, and integrated line intensity for each of the lines imaged. For the ¹²CO $J = 2 \rightarrow 1$ beam size ($6.49'' \times 2.51''$), the flux density to brightness temperature conversion is 0.71 Jy K⁻¹. The SMA-measured line ¹²CO $J = 2 \rightarrow 1$ emission morphology and line fluxes (see §3) are overall consistent with those measured with the single-dish SEST (see Sahai et al. 1990, their Fig. 2), indicating that the SMA data do not suffer from significant interferometric flux losses. We also generated a continuum image using all of the bandwidth free of strong spectral lines, with an effective frequency of 228.7 GHz. This image has an rms noise of 4.2 mJy beam⁻¹ and shows no significant features in the central region of uniform noise.

3. RESULTS

Channel maps obtained from the ¹²CO $J = 2 \rightarrow 1$ image cube are presented Fig. 1; channel maps for ¹³CO $J = 2 \rightarrow 1$ and CN $N = 2 \rightarrow 1$ are presented in Appendix A. In Fig. 2, we display velocity-integrated (moment 0) images of ¹²CO $J = 2 \rightarrow 1$, ¹³CO $J = 2 \rightarrow 1$, and CN $N = 2 \rightarrow 1$ line emission. The corresponding respective emission line profiles, obtained by spatially integrating the SMA image cubes within a $\sim 33''$ radius region centered on and encompassing the bright central molecular ring, are presented in Fig. 3. The spectra indicate that the nebular systemic velocity is ~ -25 km s⁻¹, consistent with the single-dish SEST results (Sahai et al. 1990). Table 1 lists the integrated line intensities obtained from the spectra. The CN radical is here detected for the first time in NGC 3132. Neither C¹⁸O nor continuum emission were detected.

It is immediately apparent from Fig. 1 and Fig. 2 that the brightest mm-wave molecular emission arises from the main ring of the nebula, as previously established by the SEST ¹²CO(2-1) mapping (Sahai et al. 1990). However, as we describe in detail below, the $\sim 5''$ resolution SMA interferometric mapping elucidates various fundamental aspects of the structure of ¹²CO(2-1) emission that could not have been ascertained from those previous ($\sim 22''$ resolution) single-dish SEST mapping observations.

The ¹²CO(2-1) emission is detected over LSR velocities ranging from -51 km s⁻¹ to $+3$ km s⁻¹ (Fig. 3), with the bulk of the ¹²CO emission arising from the bright central ring at velocities between roughly -40 km s⁻¹ and -5 km s⁻¹ (Fig. 1). The projected semimajor and semiminor axes of this main, bright, elliptical CO ring, as deduced from the velocity-integrated (moment 0) ¹²CO(2-1) image (Fig. 2, left), are $\sim 25''$ ($\sim 18,500$ au, assuming $D = 754$ pc) and $\sim 18''$ ($\sim 13,300$ au), respectively, with the elliptical ring oriented at position angle of approximately 330° (as measured E from N).

The ¹²CO channel maps (Fig. 1) furthermore demonstrate that the more highly blueshifted and redshifted features, centered at -50 km s⁻¹ and 0 km s⁻¹, respectively (and appearing as weak “satellite peaks” in the ¹²CO(2-1) spectrum; Fig. 3), appear to arise from compact regions within this main ring rather than from exterior jets or ansae. The CN emission (Fig. 2, right) displays the same basic (ring) emission morphology, but the signal-to-noise ratio is relatively poor and hence the detected emission is limited to velocities between roughly -40 km s⁻¹ and -12 km s⁻¹, while the (still weaker) ¹³CO emission is restricted to a still smaller velocity range (Fig. 3).

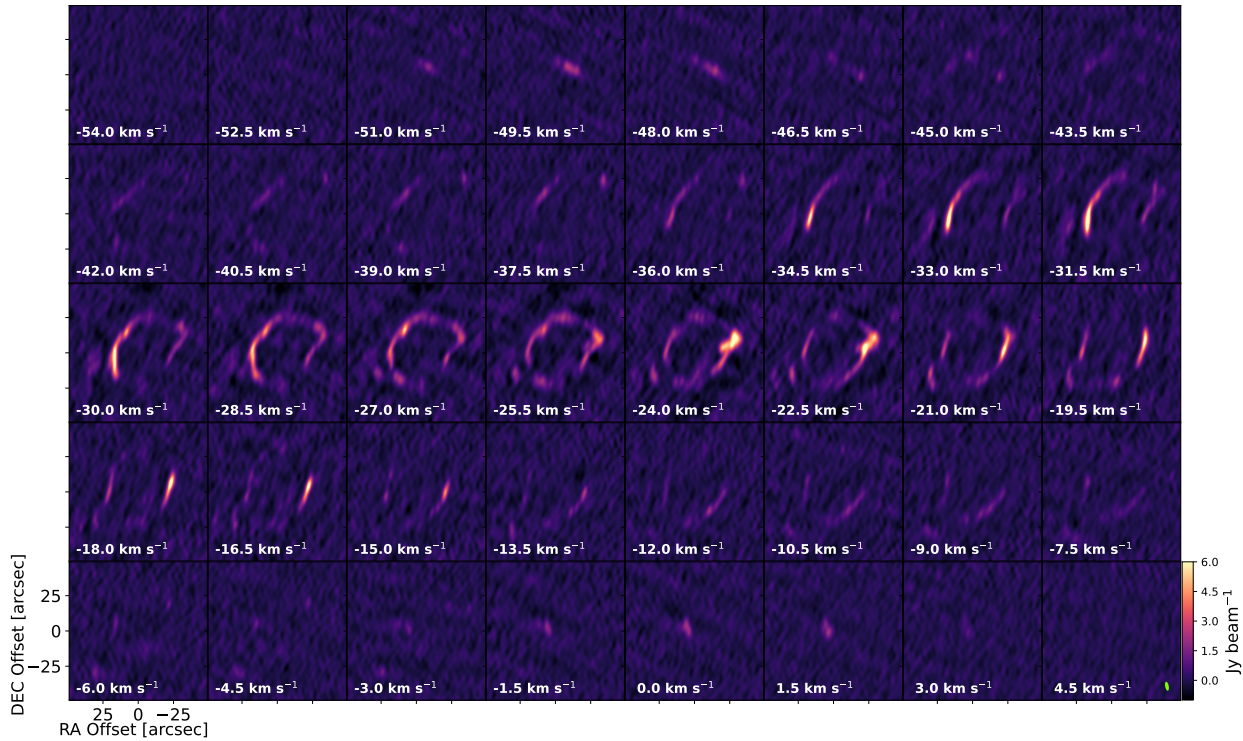


Figure 1. SMA channel maps of $^{12}\text{CO}(2-1)$ emission from NGC 3132.

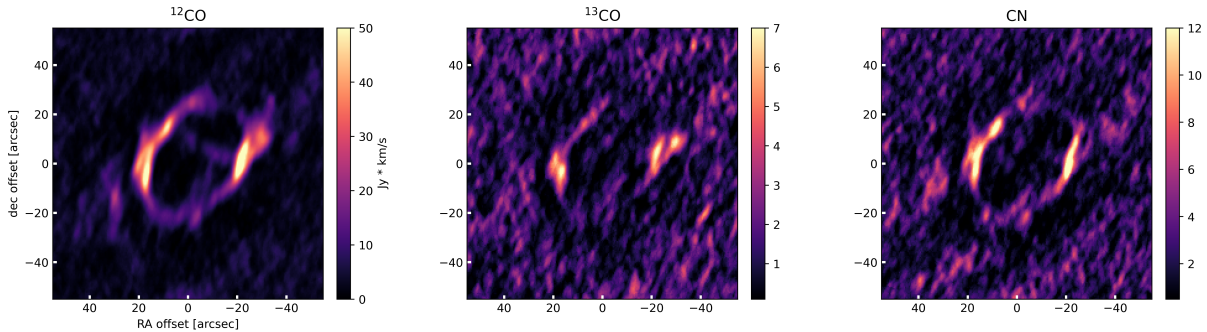


Figure 2. From left to right, velocity-integrated (moment 0) images of $^{12}\text{CO}(2-1)$, $^{13}\text{CO}(2-1)$ and $\text{CN}(2-1)$ emission, respectively, from NGC 3132 obtained from the SMA image cubes. The $^{13}\text{CO}(2-1)$ and $\text{CN}(2-1)$ moment 0 images were generated by rejecting image cube spaxels with values less than the rms noise in the data cube (see Table 1).

3.1. Comparison with archival JWST H_2 imaging

In the upper panels of Fig. 4, we compare the archival ERO JWST/NIRCam $2.12\ \mu\text{m}$ H_2 image of NGC 3132 and the SMA $^{12}\text{CO}(2-1)$ moment 0 image. It is apparent that there is a close morphological correspondence between the two images, despite their sharply contrasting spatial resolution ($\sim 0.2''$ and $\sim 5''$, respectively); the brightest near-IR H_2 and mm-wave ^{12}CO are spatially coincident, and the main, bright ring appears bifurcated in the E-W direction in both images. In the lower panels of Fig. 4, we display spectrally integrated velocity slices through the $^{12}\text{CO}(2-1)$ image cube, overlaid on the SMA moment 0 image (lower left) and JWST H_2 image (lower right). These overlays reveal that the E-W spatial bifurcation of the bright ring has a corresponding velocity bifurcation, wherein the blueshifted (approaching) ring component is spatially offset to the west of the redshifted (receding) ring component. This resolution of the central

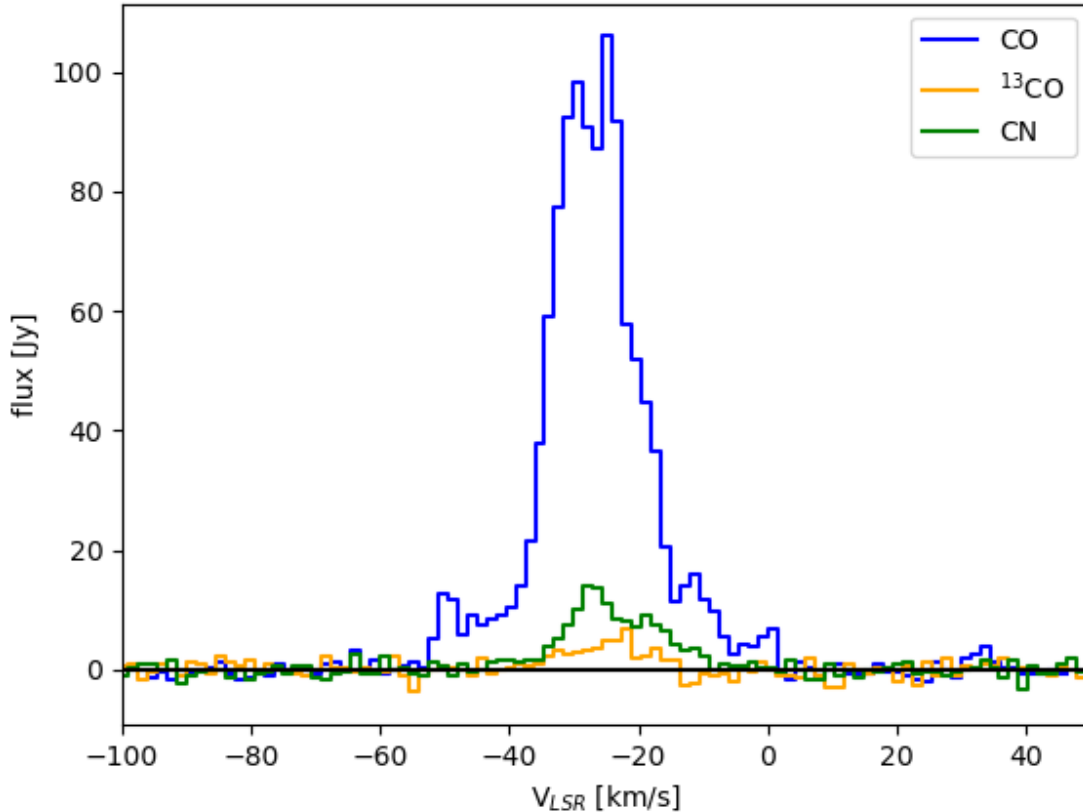


Figure 3. Spectra of $^{12}\text{CO}(2-1)$, $^{13}\text{CO}(2-1)$ and $\text{CN}(2-1)$ emission from NGC 3132 obtained by integrating the SMA image cubes within a $\sim 33''$ radius region centered on and encompassing the bright central molecular ring. The nebular systemic velocity is $\sim -25 \text{ km s}^{-1}$.

ring into distinct spatial and velocity components suggests the ring possesses an overall cylindrical structure, and is viewed at low inclination and slightly tilted along the E–W direction with respect to the line of sight.

Fig. 4 further demonstrates that the most highly blueshifted and redshifted features (knots) detected in the $^{12}\text{CO}(2-1)$ mapping correspond to distinct H_2 filaments that are projected within the main ring, and appear to cut across the nebula to the northwest and southeast of the central (visual binary) star. The northwest H_2 filament is evidently somewhat more spatially extended and coherent than the southeast H_2 filament and, correspondingly, the blueshifted ^{12}CO knot is brighter and more extended than the redshifted ^{12}CO knot.

3.2. Position-velocity images

In Fig. 5, we display three views of the SMA $^{12}\text{CO}(2-1)$ data cube, as integrated (collapsed) along each of the three cube axes. The velocity-integrated (moment 0) image is displayed in the top frame, while position-velocity (P–V) images collapsed (integrated) along the RA and declination axes are displayed in the two panels below the moment 0 image. In Fig. 6 (top row), we present P–V images obtained by spatially integrating slices of width $20''$ through the SMA $^{12}\text{CO}(2-1)$ data cube along position angles (PAs) of 60° and 150° , corresponding to the minor and major axes of the main ring of NGC 3132, respectively.

These P–V images reveal the three-dimensional structure of the NGC 3132 molecular emission. Specifically, the RA-collapsed P–V image (Fig. 5, middle panel) demonstrates that the main, bright ring seen in the near-IR H_2 (JWST) and mm-wave $^{12}\text{CO}(2-1)$ (SMA moment 0) imaging — hereafter Ring 1 — indeed has a P–V morphology consistent with an expanding ring. The decl.-collapsed P–V image (Fig. 5, bottom panel) shows that its eastern

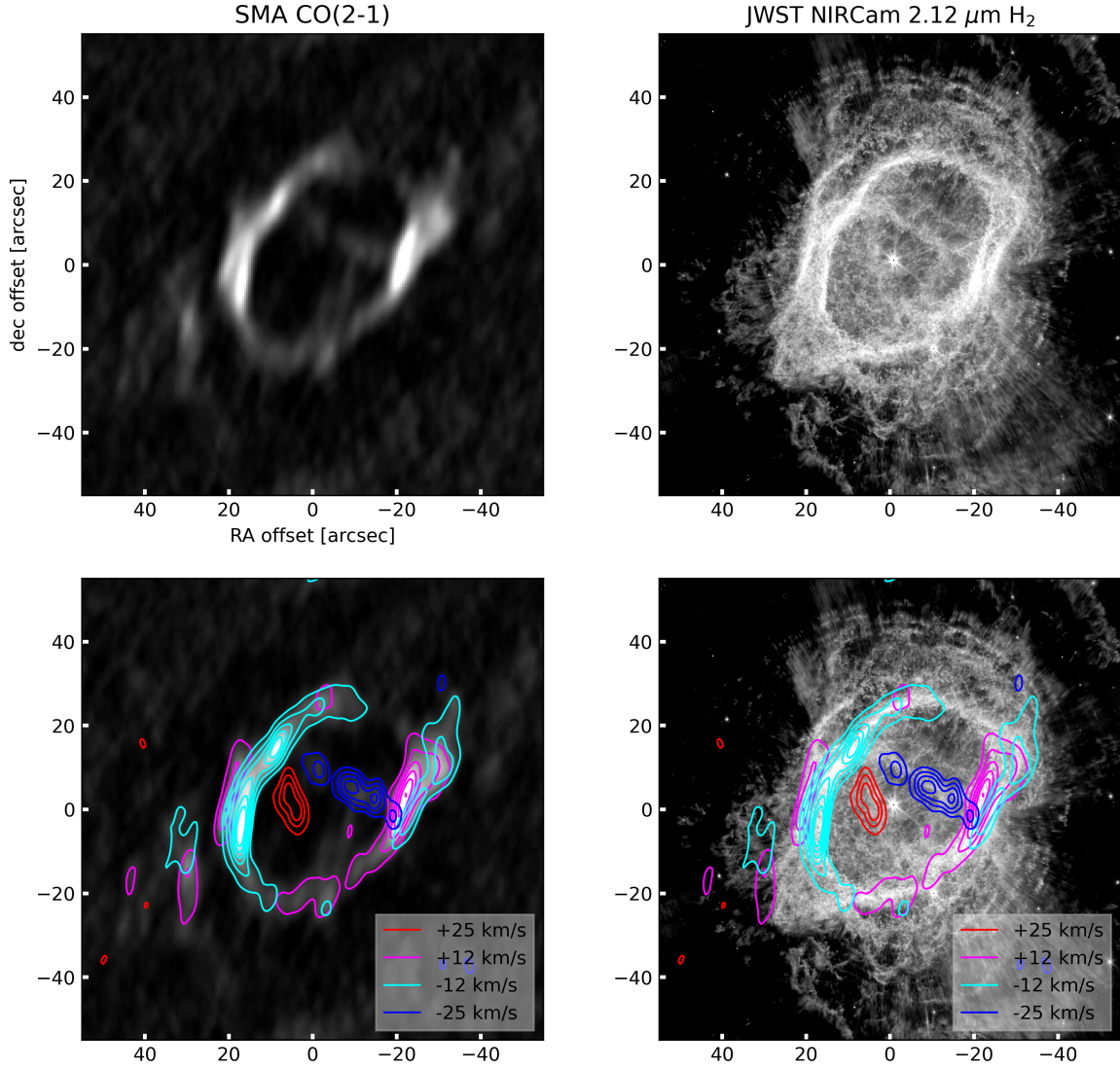


Figure 4. Comparison of JWST/NIRCam and SMA imaging of NGC 3132. Top left: velocity-integrated (moment 0) SMA $^{12}\text{CO}(2-1)$ image. Top right: JWST/NIRCam $2.12\ \mu\text{m}\ \text{H}_2$ image. Bottom left: contours of $^{12}\text{CO}(2-1)$ emission integrated over selected velocity ranges overlaid on the $^{12}\text{CO}(2-1)$ moment 0 image. The (four) velocity ranges, which are labeled with their central velocities with respect to systematic (i.e., -25 , -12 , $+12$, and $+25\ \text{km s}^{-1}$), correspond to LSR velocity ranges of -52 to $-46\ \text{km s}^{-1}$, -40 to $-25\ \text{km s}^{-1}$, -25 to $-10\ \text{km s}^{-1}$, and -2 to $+3\ \text{km s}^{-1}$, respectively. Bottom right: the same sets of velocity-resolved $^{12}\text{CO}(2-1)$ emission contours overlaid on the JWST/NIRCam H_2 image.

edge is approaching, hence, tilted toward the observer, and its western edge is receding, hence, tilted away from the observer. This P–V image and that obtained from the cut through the data cube along along PA 60° (Fig. 6, right panel) furthermore demonstrate that the minor axis of Ring 1 is tilted in velocity space by $\sim 10\ \text{km s}^{-1}$, i.e., that the line-of-sight blueshifted and redshifted (approaching and receding) velocities of the limbs of the ring are $\sim 5\ \text{km s}^{-1}$. In contrast, the P–V image obtained from the major-axis cut through Ring 1 shows essentially no velocity tilt (Fig. 6, middle panel), indicating that this line through the ring major axis, along PA 150° , represents the intersection of the plane of Ring 1 with the plane of the sky.

The P–V images in Fig. 5 and Fig. 6 (top row) also reveal the velocity coherence of the clumpy molecular emission structures that are seen projected within Ring 1. In particular, the declination-collapsed P–V image (Fig. 5, bottom panel) and minor-axis P–V image in Fig. 6 (top right panel) show that the high-velocity clumps seen in Fig. 4 (lower

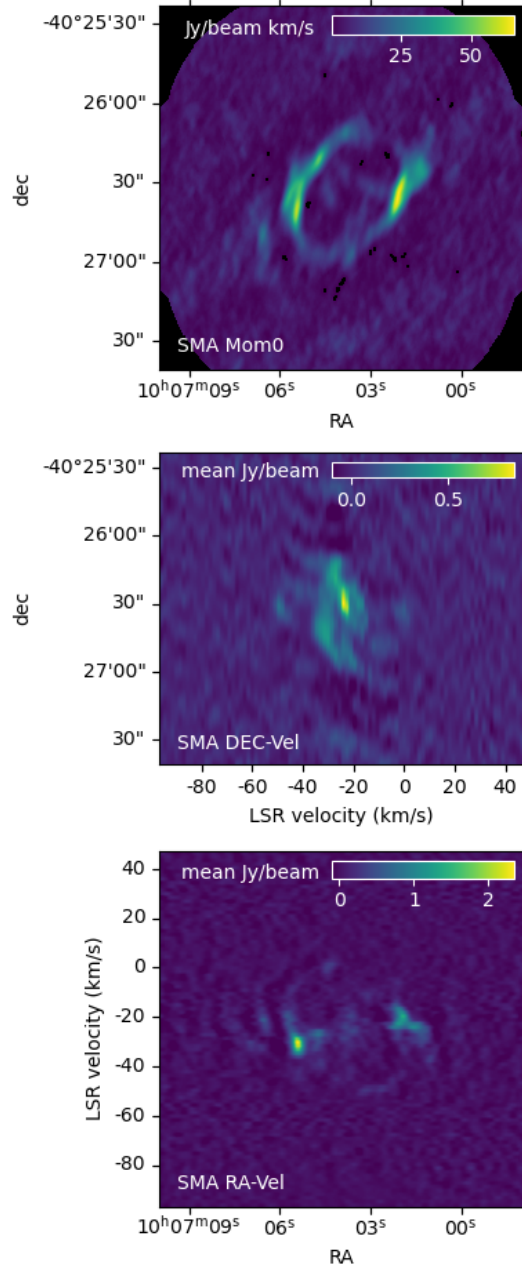


Figure 5. Three views of the SMA $^{12}\text{CO}(2-1)$ data cube. Top: the noise-clipped moment 0 image. Middle and bottom: position-velocity (P-V) images obtained by “collapsing” the data cube along the RA and declination axes, respectively. The position-integrated P-V images have been constructed so as to exclude P-V frames lying outside of the spectral extraction region used for Fig. 3.

panels) are in fact the brightest portions of what appears to be a continuous ring structure in P–V space. This second, expanding ring of molecular gas within NGC 3132 is hereafter referred to as Ring 2.

The SMA ^{12}CO moment 0 images and P–V diagrams (Fig. 6) furthermore demonstrate that Ring 1 and Ring 2 have very different inclinations with respect to the line of sight. The symmetry axis of (bright) Ring 1 is evidently viewed at low to intermediate inclination; specifically, its inclination is constrained to lie between $\sim 15^\circ$ and $\sim 45^\circ$. The lower limit on Ring 1’s inclination is obtained from its $\sim 10 \text{ km s}^{-1}$ tilt in velocity space (i.e., the $\sim 5 \text{ km s}^{-1}$ blueshift/redshift of the ring limbs; see above) under the assumption that its expansion velocity is identical to that

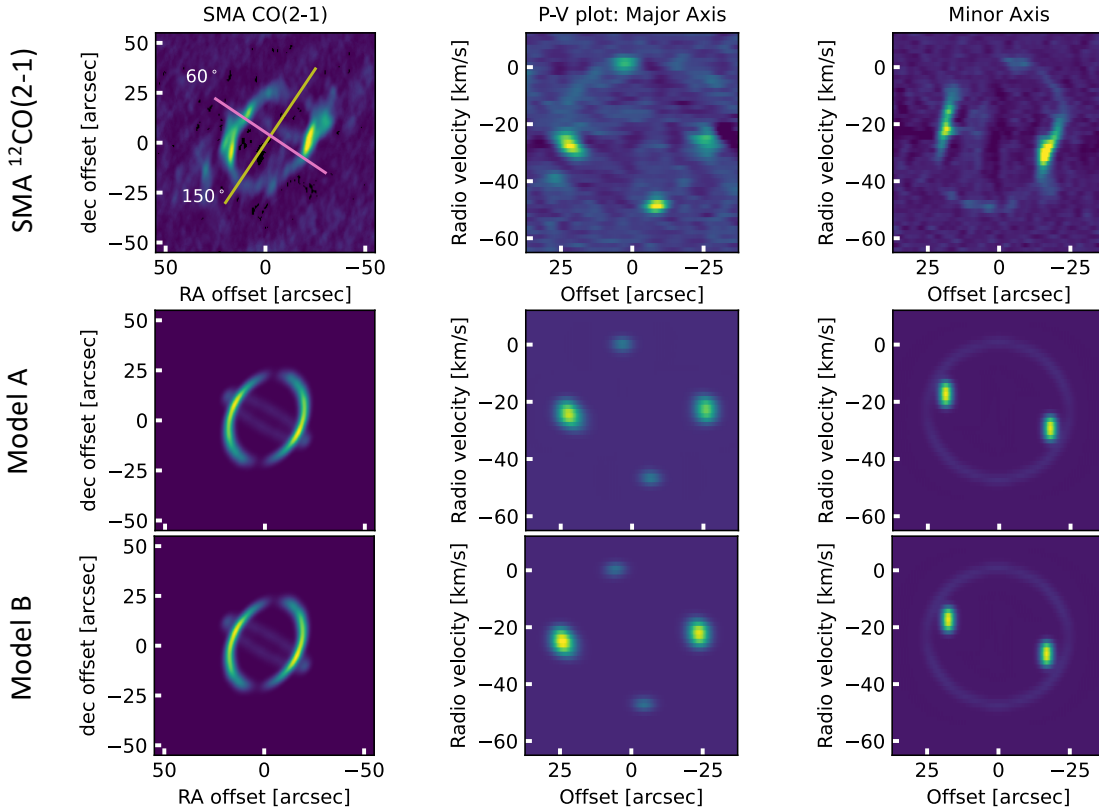


Figure 6. *Top row:* Position-velocity (P-V) images of $^{12}\text{CO}(2-1)$ emission for directions along the minor and major axes of the main ring of NGC 3132 (middle and right panels), respectively, obtained by spatially integrating slices of width $20''$ along position angles 60° and 150° . These positions of these cuts are shown in the left panel as magenta and yellow lines, respectively, overlaid on the $^{12}\text{CO}(2-1)$ moment 0 image). *Middle row:* The corresponding moment 0 and P-V images for the Model A, the 2-ring model structural invoking an elliptical Ring 1 that is viewed at an inclination of 20° . *Bottom row:* The corresponding moment 0 and P-V images for Model B, the 2-ring structural model wherein Ring 1’s dynamical age is $2.5\times$ that of Ring 2 and is viewed at an inclination of 45° . Note the similarity of the two models, which demonstrates the degeneracy of the model parameters. See Appendix B.

of Ring 2 ($\sim 25 \text{ km s}^{-1}$), while the upper limit is obtained from Ring 1’s observed (projected) major/minor axis ratio (~ 1.4).

In contrast, the (fainter) Ring 2 is viewed nearly edge-on, and appears to be oriented such that its major axis (along position angle $\sim 60^\circ$) is nearly orthogonal to that of Ring 1 (position angle of roughly 330°). The inclination of Ring 2, as obtained from its major/minor axis ratio – which we infer to be ~ 4.5 , based on the moment 0 and P-V images in Fig. 6 (top row) — is $\sim 78^\circ$. The full velocity extent of Ring 2 in the P-V images is $\sim 50 \text{ km s}^{-1}$ which, given its near edge-on orientation, implies an expansion velocity of $\sim 25 \text{ km s}^{-1}$. Assuming that the physical (linear) size of Ring 2 is similar to that of Ring 1 (i.e., radius of $\sim 18500 \text{ au}$), the dynamical age of Ring 2 is $\sim 3700 \text{ yr}$.

4. DISCUSSION

4.1. CO isotopologue and $^{12}\text{CO}/\text{CN}$ line ratios: implications for progenitor mass

The $^{12}\text{CO}(2-1)/^{13}\text{CO}(2-1)$ and $^{12}\text{CO}(2-1)/\text{CN}(2-1)$ integrated intensity line ratios measured here for NGC 3132, $\sim 48 (\pm 25\%)$ and $\sim 9 (\pm 10\%)$, respectively, (Table 1) are somewhat larger than measured by Bachiller et al. (1997) for the analogous (Ring-like) molecule-rich PNe NGC 6720 ($^{12}\text{CO}(2-1)/^{13}\text{CO}(2-1) \sim 22$; $^{12}\text{CO}(2-1)/\text{CN}(2-1) \sim 4$) and NGC 6781 ($^{12}\text{CO}(2-1)/^{13}\text{CO}(2-1) \sim 17$; $^{12}\text{CO}(2-1)/\text{CN}(2-1) \sim 6$). If both the $^{12}\text{CO}(2-1)$ and $^{13}\text{CO}(2-1)$ lines are optically thin, as was inferred for NGC 6720 and NGC 6781 (Bachiller et al. 1997) then, neglecting chemical fractionation effects, the spatially and spectrally integrated $^{12}\text{CO}(2-1)/^{13}\text{CO}(2-1)$ line ratio should directly yield a

measurement of the $^{12}\text{C}/^{13}\text{C}$ isotope ratio within the molecular envelope of NGC 3132. The inferred value, $^{12}\text{C}/^{13}\text{C} \sim 50$, is consistent with the initial mass inferred for the progenitor star (i.e., $\sim 2.9 M_{\odot}$; De Marco et al. 2022), given the predictions of models of surface AGB isotope yields (Karakas & Lugaro 2016). Specifically, the Karakas & Lugaro (2016) models predict AGB surface $^{12}\text{C}/^{13}\text{C}$ ratios in the range ~ 30 to ~ 80 for progenitor masses in the range $2\text{--}4 M_{\odot}$ at near-solar metallicity. The relatively weak CN emission relative to ^{12}CO is also consistent with the relatively low (<1.0) N/O ratios expected at the surfaces of AGB stars descended from solar metallicity progenitors in this mass range, according to the Karakas & Lugaro (2016) models.

4.2. CO column densities and molecular gas mass

To obtain ^{12}CO column densities and (hence) estimate the total molecular gas mass of NGC 3132 from the SMA $^{12}\text{CO}(2\text{--}1)$ data, we use the publicly available RADEX radiative transfer code¹ (van der Tak et al. 2007). For an assumed molecular gas kinetic temperature of $T_k = 30$ K (see, e.g., Bachiller et al. 1997) and H_2 number density of $n_{\text{H}_2} = 10^6 \text{ cm}^{-3}$, RADEX calculations indicate that the measured SMA antenna temperatures — which range from $\sim 0.6 \text{ Jy beam}^{-1}$ (~ 1.0 K) to $\sim 6.5 \text{ Jy beam}^{-1}$ (~ 10 K) across the individual channel maps (Fig. 1) — correspond to a range in ^{12}CO column densities from $N_{\text{CO}} \sim 7 \times 10^{14} \text{ cm}^{-2}$ to $\sim 7 \times 10^{15} \text{ cm}^{-2}$. The ^{12}CO emission is predicted to be optically thin ($\tau_{^{12}\text{CO}} < 0.5$) over this domain of N_{CO} for the foregoing assumptions for T_k and n_{H_2} . For significantly smaller assumed values of T_k and n_{H_2} , RADEX predicts that the emission would become marginally to very optically thick, which would be inconsistent with the relatively large measured value of $^{12}\text{CO}(2\text{--}1)/^{13}\text{CO}(2\text{--}1) \approx 48$ (§ 4.1).

The approximate mean of the velocity-integrated (moment 0 image) ^{12}CO line intensities is $\sim 30 \text{ K km s}^{-1}$. Given the foregoing, we hence infer that the mean integrated ^{12}CO column density along a line of sight through the CO-emitting regions of the nebula is $\sim 2 \times 10^{16} \text{ cm}^{-2}$. For purposes of a rough estimate of the total molecular mass of NGC 3132, we adopt this mean value of N_{CO} . Approximating the ^{12}CO emitting region of NGC 3132 as an annulus of radius $20''$ ($15,000 \text{ au}$) and thickness $3''$ (2250 au), we find that total number of CO molecules is $N(\text{CO}) \sim 10^{51}$. This estimate for $N(\text{CO})$ is very similar to (within $\sim 30\%$ of) that obtained by Sahai et al. (1990). To convert $N(\text{CO})$ to an H_2 mass then requires an assumption for the CO abundance relative to H_2 , $[\text{CO}]/[\text{H}_2]$, which is a notoriously uncertain quantity (e.g., Bolatto et al. 2013; Bisbas et al. 2015; Yu et al. 2017, and references therein). Adopting a plausible range of $[\text{CO}]/[\text{H}_2]$ that is appropriate for evolved star envelopes — i.e., between 10^{-4} and 10^{-5} (see discussion in Sahai et al. 1990) — we obtain an estimated total molecular gas mass of between $\sim 0.015 M_{\odot}$ and $\sim 0.15 M_{\odot}$ for NGC 3132.

4.3. The structure of NGC 3132’s molecular exoskeleton

The SMA data indicate that the Southern Ring’s main, bright, molecule-rich ring (Ring 1) is indeed a ring that is viewed at low to intermediate inclination, as opposed to a limb-brightened shell, in terms of its intrinsic (physical) structure (§ 3). This conclusion, which is consistent with the results of the previous single-dish (SEST) CO mapping (as interpreted by Sahai et al. 1990), is supported by our empirical modeling of the ^{12}CO data (Appendix B and Fig. 6). Evidently, the main, CO-bright reservoir of molecular gas in NGC 3132 is largely confined to the equatorial and lower-latitude regions of the nebula. The SMA $^{12}\text{CO}(2\text{--}1)$ mapping results are hence consistent with those of previous surveys of H_2 and CO emission from PNe. As noted earlier, such molecular emission-line surveys have established that the vast majority of molecule-rich PNe are intrinsically bipolar in structure, with the bulk of the molecular gas residing in equatorial tori (Kastner et al. 1996; Huggins et al. 1996, 2005). The geometries of these toroidal or ring structures are conducive to self-shielding and dust-shielding of the molecules against the PN central star’s intense, dissociating UV irradiation (Zuckerman & Gatley 1988). Our confirmation that the nebula’s main, bright ring is intrinsically ring-like in structure, as opposed to a limb-brightened shell, therefore strongly supports the hypothesis of Sahai et al. (1990) that NGC 3132 is (or at least was) in fact a bipolar nebula with polar axis viewed at low to intermediate inclination with respect to the line of sight.

Indeed, the SMA data resolve Ring 1 into distinct spatial and velocity components, with indications of point-symmetric structure (Fig. 4), suggesting that this $^{12}\text{CO}(2\text{--}1)$ emission arises from both an equatorial torus and the bases of polar lobes. The empirical model presented in Appendix B, in which Ring 1 is modeled as a simple cylindrical structure, does not account for these features (see, e.g., the right-hand column of Fig. 6). Ring 1 hence may constitute the low-latitude portions of the twin-cone (“Diabolo”) geometry that has been proposed to explain the nebula’s ionized

¹ <https://home.strw.leidenuniv.nl/moldata/radex.html>

gas morphology and kinematics (Monteiro et al. 2000; Monreal-Ibero & Walsh 2020). The polar lobes have presumably expanded far enough into the ISM over the $\gtrsim 3000$ yr (dynamical) lifetime of NGC 3132’s ring system (see below) that any residual lobe molecular gas is now difficult to detect. However, it is possible that some of the extended (halo) H_2 emission seen both within and outside of the main bright molecular ring in JWST imaging arises from such polar lobe material. If so, then this polar lobe H_2 emission morphology would appear to be in conflict with the Diabolo model, as the brightest “halo” H_2 emission in the JWST images is more or less aligned with the major axis of Ring 1 (Fig. 4, top right panel), whereas the Diabolo model requires the projected lobe emission to be aligned with the ring’s minor axis (see, e.g., Fig. 5 of Monteiro et al. 2000). We note that the SMA data also reveal weak $^{12}\text{CO}(2-1)$ emission exterior to Ring 1, in the form of a faint arc extending toward the ESE that has an even fainter potential counterpart to the WNW (see, e.g., Fig. 4, top left panel). These faint molecular halo structures warrant confirmation and followup via deeper, wider-field CO mapping.

Surprisingly, the data further reveal that the nebula also appears to harbor a second, dust-rich molecular ring (Ring 2) — detected in (dust) absorption, in low-excitation emission lines (Monteiro et al. 2000; Monreal-Ibero & Walsh 2020; De Marco et al. 2022), in H_2 (De Marco et al. 2022), and (now) in $^{12}\text{CO}(2-1)$ — that appears to lie nearly perpendicular to Ring 1, at least as seen in projection in the SMA $^{12}\text{CO}(2-1)$ moment 0 image. Under the assumption that Ring 2’s radius is similar to the semimajor axis of Ring 1 (18,500 au; §3), the measured expansion velocity of Ring 2 (25 km s $^{-1}$; §3.2) implies that the dynamical age of Ring 2 is ~ 3700 yr.

Motivated by these results, we describe in Appendix B a simple geometrical model for the structure of NGC 3132’s $^{12}\text{CO}(2-1)$ emission regions consisting of two rings with sharply contrasting inclinations with respect to the line of sight. This simple two-ring model of NGC 3132’s molecular exoskeleton greatly oversimplifies aspects that are readily apparent in the SMA observations of NGC 3132, such as the line-of-sight velocity extent and structure of its main, bright $^{12}\text{CO}(2-1)$ ring (Ring 1) and the highly uneven (knotty) $^{12}\text{CO}(2-1)$ brightness distributions of both rings. Notwithstanding its simplicity, this empirical model can reproduce the apparent two-ring structure of the $^{12}\text{CO}(2-1)$ emission that is seen in velocity-integrated and P-V images obtained from the SMA data (Fig. 6 and Fig. 10) and in volumetric views of the data cube itself (Fig. 11), as well as the main features and basic shape of the SMA $^{12}\text{CO}(2-1)$ line profile (Fig. 12).

Based on the analysis presented in Appendix B, we furthermore conclude that Ring 1 either is intrinsically elliptical and is viewed only $\sim 20^\circ$ from pole-on (Model A); or, if Ring 1 is perfectly circular and viewed more obliquely — specifically, at inclination $\sim 45^\circ$, as indicated by its ellipticity — that its expansion velocity is ~ 2.5 times smaller than that of Ring 2 (Model B). The parameters of these two alternative models (i.e., ring inclinations, expansion velocities, dynamical ages, and major/minor axis ratios) are listed in Table 2. Synthetic moment 0 and P–V images, where the latter have been extracted from cuts through the Model A and Model B along PAs of 60° and 150° , are presented in the middle and bottom rows of panels in Fig. 6, respectively.

As in the comparisons between SMA ^{12}CO data and models presented in Appendix B, Fig. 6 demonstrates that Models A and B both well reproduce the essential aspects of the basic morphologies of the SMA moment 0 and P–V images (top row of Fig. 6), despite the fundamental differences between the two models. In particular, Model B requires the dynamical ages of the two rings to be very different — i.e., ~ 3700 yr (Ring 2) vs. ~ 9000 yr (Ring 1) — whereas Model A relies on the assumption that their dynamical ages are identical. Furthermore, in Model A, the symmetry axes of the two rings are nearly orthogonal to one another, whereas in Model B, their inclinations differ by $\sim 60^\circ$. The striking similarity of the moment 0 and P–V projections of these two fundamentally different two-ring model realizations hence emphasizes the degeneracy of the model parameters (ring inclinations, ellipticities, and dynamical ages).

The degeneracy between Models A and B can be broken via direct measurement of the expansion proper motion of Ring 1 from multi-epoch HST or JWST images, once available; such a measurement of its projected expansion velocity will firmly establish Ring 1’s dynamical age. Meanwhile, for purposes of the following discussion of the potential shaping processes that have generated the present-day NGC 3132, we adopt Model A, on the basis of its relative simplicity and the various independent lines of evidence that favor a dynamical age significantly less than ~ 9000 yr for the ionized nebula (see, e.g., De Marco et al. 2022). We stress, however, that we cannot yet rule out Model B based on the data at hand.

4.4. Implications for the shaping of NGC 3132 by its central star system

The main, bright molecular ring or torus structure that dominates the $^{12}\text{CO}(2-1)$ emission from NGC 3132 (Ring 1) would appear to closely resemble the molecular tori associated with “classical” pinched-waist bipolar nebulae, with perhaps the best example being NGC 6302 (Santander-García et al. 2017). That nebula, like NGC 3132, harbors a CO-bright equatorial torus with some CO emission extending into the polar lobes. There is broad consensus that the shaping of PNe characterized by such profound bipolar (pinched-waist plus lobe) structures requires a close (interacting) binary companion to the central star (see, e.g., De Marco 2009; Jones & Boffin 2017; Kastner et al. 2022, and references therein).

However, the apparent presence of a second, fainter, nearly pole-on molecular ring in NGC 3132 (Ring 2) would appear to complicate this (relatively simple) interpretation. That is, the formation and apparent near-simultaneous ejection of two nearly orthogonal molecular rings implied by Model A appears difficult to reconcile with a model of NGC 3132 as a nearly pole-on bipolar nebula shaped by a central, interacting binary star system. While a definitive explanation for the formation of such a two-ring structure is beyond the scope of this paper, we offer a general scenario here.

If the rings indeed have very similar dynamical ages then — given their similar, AGB-like expansion velocities — we would conclude that Ring 2 is the remnant of the same massive ejection of molecular gas from the AGB progenitor that generated Ring 1. It is possible that this rapid mass loss event terminated the progenitor star’s AGB evolution. The bulk of the AGB envelope ejection was evidently focused along the equatorial plane, forming Ring 1, but the rapid (and perhaps terminal) ejection of the AGB star’s molecule-rich envelope — as traced in $^{12}\text{CO}(2-1)$ in the form of Ring 2 — appears to have been overall quasi-spherical or ellipsoidal in geometry. This would be consistent with recent 3D morpho-kinematic modeling of long-slit spectroscopy of [N II] emission, which indicates that the central ionized gas cavity within NGC 3132 has a prolate ellipsoidal shell structure with its major axis oriented at $\sim 30^\circ$ with respect to the line of sight (De Marco et al. 2022).

It would then remain to explain the double-ring — as opposed to closed ellipsoidal — structure of the residual molecular gas that is apparent in the SMA $^{12}\text{CO}(2-1)$ data cube. One possibility is that, after its ejection, the initially ellipsoidal molecular shell was quickly disrupted by a rapid-fire series of misaligned jet pairs emanating from the central multiple star system. This process might leave only a narrow (quasi-circular or elliptical) region of the polar lobes “untouched,” and this region could take the form of Ring 2, i.e., a second molecular ring oriented nearly perpendicular to the nebula’s equatorial (molecular) torus.

Such a scenario, though highly speculative, would be consistent with the evidence for multiple, misaligned (possibly precessing) jet pairs imprinted in the inferred structure of NGC 3132’s central ionized cavity and halo (Monreal-Ibero & Walsh 2020; De Marco et al. 2022). The presence of such intermittent, wobbling (possibly precessing) jets would strongly suggest that the mass-losing progenitor was a member of an interacting triple (as opposed to double) star system (De Marco et al. 2022, and references therein). As detailed in De Marco et al. (2022), the likelihood that the mass-losing AGB progenitor was a member of a hierarchical multiple system² is further supported by JWST’s detection of both a thermal IR excess from a dust disk at the central star (see also Sahai et al. 2023) and a ring or spiral pattern in the nebula’s extensive H_2 halo.

The foregoing general scenario, wherein the AGB and post-AGB mass loss leading to PN formation rapidly progresses from quasi-spherical to highly collimated and perhaps somewhat chaotic, is of course not new; such a model has long been invoked to explain the ongoing, rapid structural metamorphosis of young bipolar and multipolar PNe (e.g., Sahai & Trauger 1998; Rechy-García et al. 2020). We further note that the superimposed structures observed in the young PN NGC 7027 — a halo ring system and equatorial molecular torus surrounding an inner elliptical shell that has recently been punctured by a set of (three) misaligned jet pairs (Moraga Baez et al. 2023) — would appear to make this object a particularly close analog to NGC 3132. Indeed, NGC 3132 may offer a glimpse into the future of the disruptive processes now underway in very young PNe such as NGC 7027.

5. CONCLUSIONS

We have obtained Submillimeter Array (SMA) mapping of $^{12}\text{CO } J = 2 \rightarrow 1$, $^{13}\text{CO } J = 2 \rightarrow 1$, and CN $N = 2 \rightarrow 1$ emission from the Ring-like planetary nebula (PN) NGC 3132. Recent JWST (Early Release Observation) infrared

² The A-type visual binary companion is too widely separated from the mass-losing progenitor to have influenced its mass loss geometry, so would represent a distant (non-interacting) fourth component of such a multiple system.

imaging of NGC 3132 has revealed the structure of its H₂ emission region in unprecedented detail (De Marco et al. 2022), but provided no information concerning its molecular gas kinematics. The velocity-resolved SMA observations presented here, which constitute the first mm-wave interferometric mapping of molecular line emission from the nebula, provide additional insight into the structure of NGC 3132’s molecular envelope. Our main results and conclusions are as follows.

- The bulk of the mm-wave ¹²CO(2–1) emission from NGC 3132 arises from the PN’s bright central ring system, with a velocity-integrated morphology closely resembling that of the brightest regions of H₂ emission imaged in the IR regime by JWST. The CN radical, a sensitive probe of N chemistry and photodissociation processes in PNe (e.g., Bachiller et al. 1997), is here detected for the first time in NGC 3132. The velocity-integrated CN(2–1) image displays a morphology very similar to that of ¹²CO(2–1).
- We infer ¹²CO(2–1)/¹³CO(2–1) and ¹²CO(2–1)/CN(2–1) abundance ratios of ~ 50 and ~ 10 , respectively, from the measured integrated intensity ratios. These abundance ratios would appear to be consistent with the initial mass inferred for the progenitor star (i.e., $\sim 2.9 M_{\odot}$; De Marco et al. 2022), given the predictions of models of surface AGB isotope yields. The mean integrated ¹²CO column density across the emitting region is found to be $\sim 2 \times 10^{16} \text{ cm}^{-2}$, leading to an estimate for total nebular molecular (H₂) mass of between $\sim 0.015 M_{\odot}$ and $\sim 0.15 M_{\odot}$.
- The SMA data demonstrate that the Southern Ring’s main, bright, molecule-rich ring (designated Ring 1) is indeed a ring that is viewed at low to intermediate inclination, as opposed to a limb-brightened shell, in terms of its intrinsic (physical) structure. It therefore appears that the main (CO-bright) reservoir of molecular gas in NGC 3132 is confined to the low-latitude regions of the nebula. This in turn strongly suggests that the Southern Ring is, or at least was, in fact a bipolar nebula whose polar axis is inclined by $\sim 15\text{--}45^{\circ}$ with respect to our line of sight.
- The data further reveal that the nebula also harbors a second molecular (CO-emitting) ring (designated Ring 2) that is seen projected almost orthogonally to Ring 1. We show that a simplified geometrical model consisting of two expanding molecular rings can reproduce the basic, two-ring structure of the ¹²CO(2–1) emission that is seen in velocity-integrated and P-V images obtained from the SMA data, as well as the general morphology of the spatially integrated ¹²CO(2–1) line profile. This empirical modeling exercise demonstrates that if Ring 1 and Ring 2 have identical expansion velocities ($\sim 25 \text{ km s}^{-1}$) and dynamical ages ($\sim 3700 \text{ yr}$), then Ring 1 is intrinsically elliptical and is viewed only $\sim 20^{\circ}$ from pole-on. Alternatively, if Ring 1 is perfectly circular, such that its apparent ellipticity is entirely the result of viewing angle (inclination $\sim 45^{\circ}$), then its expansion velocity must be ~ 2.5 times smaller than – hence, its dynamical age ~ 2.5 times larger than — that of Ring 2.
- The apparent presence of a second, fainter, nearly edge-on “twin” to the main, bright, nearly pole-on Ring 1 would appear to complicate the (relatively simple) interpretation of the structure of NGC 3132 as a nearly pole-on bipolar nebula shaped by the gravitational influence of a single close companion to the progenitor star. We suggest that this apparent two-ring structure may be the remnant of an ellipsoidal molecular envelope of AGB ejecta that has been mostly dispersed by a series of rapid-fire but misaligned collimated outflows or jets. Such a scenario would be consistent with the hypothesis that the mass-losing AGB progenitor of NGC 3132 was a member of an interacting triple star system (De Marco et al. 2022). Detailed simulations of the dynamical effects of such multiple-star “toppling jets” systems on AGB molecular envelopes are required to test this speculative scenario for the shaping of the molecular exoskeleton of NGC 3132.

Additional (sub)mm-wave (ALMA) interferometric observations of molecular emission from NGC 3132 at higher resolution and sensitivity are necessary. Such ALMA molecular line observations are needed both to confirm and further elucidate the two-ring structure that is apparent in the SMA data and, more generally, to attempt to detect and map any cold ($\sim 30\text{--}100 \text{ K}$) molecular gas that lies within the myriad faint knots and filamentary structures imaged in near-IR (hot, $\sim 1000\text{--}3000 \text{ K}$) H₂ by JWST. Meanwhile, a second epoch of HST and/or JWST imaging would enable measurement of the projected expansion speed of the main, bright ring of the nebula (Ring 1), so as to ascertain its dynamical age and thereby test the hypothesis that the two rings mapped in CO by SMA were ejected nearly simultaneously in an AGB-terminating mass loss episode.

ACKNOWLEDGMENTS

The authors thank the anonymous referee for many helpful comments and suggestions. Research by J.K. and P.M.B. on the molecular content of planetary nebulae is supported by NSF grant AST-2206033 to RIT. R.S.'s contribution to the research described here was carried out at the Jet Propulsion Laboratory, California Institute of Technology, under a contract with NASA, and funded in part by NASA via ADAP awards, and multiple HST GO awards from the Space Telescope Science Institute. The Submillimeter Array is a joint project between the Smithsonian Astrophysical Observatory and the Academia Sinica Institute of Astronomy and Astrophysics and is funded by the Smithsonian Institution and the Academia Sinica. We recognize that Maunakea is a culturally important site for the indigenous Hawaiian people; we are privileged to study the cosmos from its summit. The *JWST* data used in this paper can be found in MAST: [10.17909/vhaw-9z45](https://mast.stsci.edu/#/search/10.17909/vhaw-9z45).

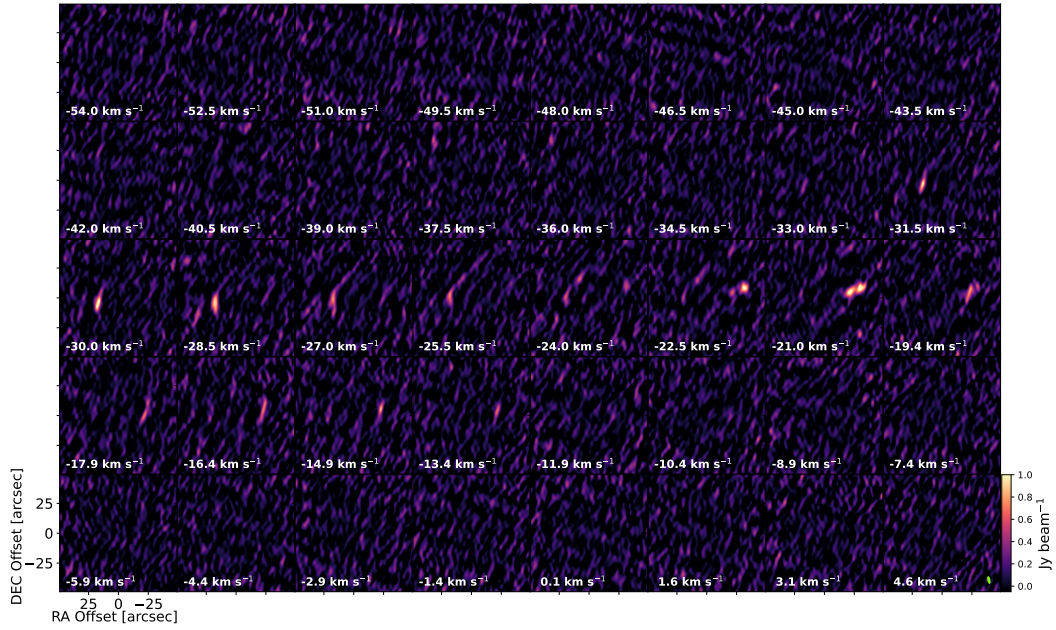
APPENDIX A: $^{13}\text{CO } J = 2 \rightarrow 1$ AND $\text{CN } N = 2 \rightarrow 1$ CHANNEL MAPS

Figure 7. SMA channel maps of $^{13}\text{CO}(2-1)$ emission from NGC 3132.

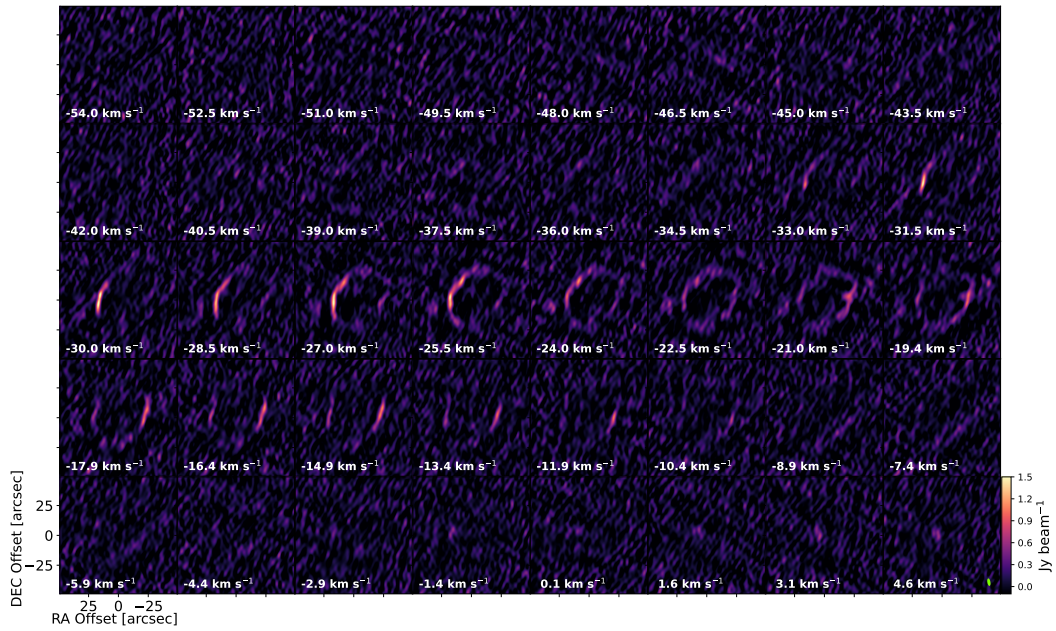


Figure 8. SMA channel maps of $\text{CN}(2-1)$ emission from NGC 3132.

Fig. 7 and Fig. 8 display channel maps for NGC 3132 as obtained from the SMA $^{13}\text{CO } J = 2 \rightarrow 1$ and $\text{CN } N = 2 \rightarrow 1$ (226.87478 GHz hyperfine component) line image cubes, respectively.

APPENDIX B: A SIMPLE GEOMETRIC MODEL

To interpret the ^{12}CO emission morphology in P–V space as revealed by the SMA data (§ 3.2), we construct a simple model of the main molecular gas structures within NGC 3132. We make no attempt to model the ^{12}CO (rotational ladder) excitation or $^{12}\text{CO}(2-1)$ photon radiative transfer; rather, the model constructed here is purely a geometrical representation of the $^{12}\text{CO}(2-1)$ emission region within NGC 3132. Motivated and constrained by the SMA $^{12}\text{CO}(2-1)$ mapping results described in § 3.2, the model we consider consists of two expanding rings of molecular gas that are viewed at significantly different orientations: a bright Ring 1, whose symmetry axis is viewed at relatively low inclination with respect to the line of sight, and a fainter Ring 2, which is viewed nearly edge-on and appears to be oriented such that its major axis (along position angle $\sim 60^\circ$, measured E from N) is nearly orthogonal to that of Ring 1 (position angle of roughly 330°). Both rings are modeled in 3D cartesian coordinates (x, y, z) as ellipses whose minor and major axes lie along x and y , respectively, and whose z dimension is scaled according to the ring’s expansion velocity. Ring 1 can be rotated around the y axis, while Ring 2 can be rotated around the x axis. These orthogonal rotations result in ellipse dimensions along x and z (Ring 1) or y and z (Ring 2) that are foreshortened and modulated, respectively, by the projection effects resulting from the rings’ inclinations.

To roughly reproduce the azimuthal asymmetry of the brighter, lower-inclination Ring 1 as seen in the SMA moment 0 CO image (Fig. 2, left), the (x, y, z) coordinates of Ring 1 are assigned intensity values ranging from 0 to 1.0, with a $\cos(2\phi + \phi_0)$ dependence on azimuthal angle ϕ and a rotation of $\phi_0 = 30^\circ$. The (fainter) Ring 2 is assigned uniform intensity values of 0.125, so as to roughly match the contribution of Ring 2 to the integrated $^{12}\text{CO}(2-1)$ spectrum (see below). Off-ring positions are assigned values of 0.

To facilitate the comparison with observations, we convolve the resulting two-ring structure with Gaussian functions approximating the asymmetric ($6.5'' \times 2.5''$) SMA beam and line spread function (3 km s^{-1} , i.e., two image cube channels). To roughly approximate the wide velocity range over which portions of Ring 1 appear to be detected (from $\sim -40 \text{ km s}^{-1}$ to $\sim -5 \text{ km s}^{-1}$; Fig. 1), the z (velocity) dimension of Ring 1 is further convolved with a boxcar convolution kernel of width 7.5 km s^{-1} . This velocity “smearing” is an attempt to model the line-of-sight extent of Ring 1, and is hence distinct from the blueshifts/redshifts due to the projected expansion velocity of Ring 1. Finally, we reproject the model cube spaxels from (x, y, z) into the equivalent SMA data cube (RA, decl., velocity) coordinate space and rotate the entire resulting image cube through a position angle of 330° , to approximate the observed (projected) rotation of Ring 1 on the sky (§ 3).

To illustrate the output of the resulting two-ring model and the comparison with the SMA ^{12}CO mapping data, we first consider two model realizations, both invoking a pair of perfectly circular rings with identical radii (18,500 au) and expansion velocities (25 km s^{-1}), hence identical dynamical ages (3700 yr). In the first realization, the inclinations of both Rings 1 and 2 are given by their major/minor axis ratios, as deduced from the SMA moment 0 ^{12}CO image. These ratios are ~ 1.4 and ~ 4.5 for Rings 1 and 2, respectively (see § 3.2), so we set their respective model inclinations to $\sim 45^\circ$ and $\sim 78^\circ$.

The resulting structural model data cube is illustrated in the center column panels of Fig. 9 in the form of a synthetic moment 0 image and synthetic P–V images obtained by “collapsing” the model image cube along the RA and declination axes. These images are presented, alongside their observational (SMA ^{12}CO data cube) counterparts, in the center and left columns of Fig. 9, respectively. It is readily apparent that the synthetic moment 0 image provides a good match to the data, as expected given that the $\sim 45^\circ$ inclination of Ring 1 in the model has been set by the degree of ellipticity of this Ring in the SMA moment 0 image. However, in the RA- and decl-collapsed P–V images, the full projected velocity extent of the model Ring 1 ($\sim 40 \text{ km s}^{-1}$) is much larger than that observed ($\sim 20 \text{ km s}^{-1}$).

In the second model realization, we attempt to qualitatively account for this discrepancy in the velocity extent of Ring 1, by moderating its inclination. We are guided by the observation that if the expansion velocity of Ring 1 is identical to that measured for Ring 2, $\sim 25 \text{ km s}^{-1}$, then the ~ 10 – 12 km s^{-1} tilt of Ring 1 in P–V space (Fig. 6, top right panel) would indeed imply that Ring 1’s inclination is only $\sim 15^\circ$. We hence reduce Ring 1’s inclination accordingly, in the second model realization. The resulting structural model data cube is illustrated in the right-hand panels of Fig. 9. As expected, this model provides an improved match to the observed RA- and decl-collapsed P–V images, but the synthetic moment 0 image (top right-hand column panel) fails to match the observed ellipticity of Ring 1 in the SMA moment 0 image (top right-hand column panel).

The data-model comparisons in Fig. 9 lead us to conclude that Ring 1 is either intrinsically elliptical in structure, or that its expansion velocity is significantly smaller — and hence its dynamical age significantly larger — than that of Ring 2. Thus, in an attempt to generate structural model data cubes that might more accurately reproduce Ring 1’s

Table 2. TWO-RING CO EMISSION MODELS: PARAMETERS

Model	Ring 1				Ring 2			
	i^a ($^\circ$)	V_e^b (km s^{-1})	age ^c (yr)	r^d	i^e ($^\circ$)	V_e^b (km s^{-1})	age ^c (yr)	r^d
A	20	25	3700	1.25	78	25	3700	1.0
B	40	10	9250	1.0	78	25	3700	1.0

NOTES:

a) Inclination of symmetry axis with respect to line of sight; b) expansion velocity; c) dynamical age; d) major/minor axis ratio.

morphology in all three SMA data cube renderings — i.e., the observed moment 0 image as well as the P–V images — we generate two additional, revised models corresponding to these two possibilities. In the first revised model (Model A), Ring 1 is elliptical, with major/minor axis ratio of 1.25 and semimajor axis of 18,500 au along the y direction, and is viewed at low inclination (20°). The expansion velocity of Ring 1 is modulated, from a maximum of 25 km s^{-1} along the major axis to 20 km s^{-1} along the minor axis, so as to maintain a uniform dynamical age of 3700 yr around the ring. In the second revised model (Model B), Ring 1 remains circular, with assumed radius of 18,500 au, but its expansion velocity is reduced to 10 km s^{-1} , corresponding to an increased dynamical age of 9250 yr. The values of the fundamental parameters of Models A and B — ring inclination, expansion velocity, dynamical age, and major/minor axis ratio — are listed in Table 2. For simplicity, the parameters of Ring 2 are held constant for the two models.

The resulting structural model data cubes are illustrated in the center and right-hand columns of Fig. 10. It is immediately apparent that both models more closely match the data than either of the models presented in Fig. 9. Comparison of volume renderings of the SMA $^{12}\text{CO}(2-1)$ data cube further support the general viability of both models; one such set of comparisons is presented in Fig. 11, where we show three example oblique views of SMA and model data cubes generated via the `Glue` software³. In both Fig. 10 and Fig. 11, Models A and B are nearly indistinguishable. Evidently, the family of 2-ring models is degenerate in terms of their possible combinations of inclination, eccentricity, and expansion velocity (or, equivalently, assumed dynamical age).

Despite the simplicity of the foregoing double-ring model — and the complexities (knots, filaments) evident in the data that are not represented in such a simple model — the side-by-side comparisons in Fig. 10 and Fig. 11 demonstrate that the two-ring model can reproduce the fundamental morphologies apparent in the data. That is, in each of the views presented in these Figures, the $^{12}\text{CO}(2-1)$ emission appears as two intersecting elliptical rings whose ellipticity (eccentricity) and points of intersection are essentially functions of data cube “viewing angle.” Because the model does not account for opacity effects — thereby implicitly representing optically thin emission — the integrated-intensity renderings of the model in Fig. 10 exhibit brightness peaks at specific locations along the two rings where each ring lies more nearly along the axis of integration (i.e., limb brightening), or where the two rings intersect. The $^{12}\text{CO}(2-1)$ data display brightness peaks in some of these same locations — compare, e.g., the bottom row of panels in Fig. 10 — despite the fact that the model does not account for local density enhancements (knots) along the rings. This supports the notion that the $^{12}\text{CO}(2-1)$ emission in Ring-like PNe like NGC 3132 is optically thin (Bachiller et al. 1997).

In Fig. 12, we present a comparison of observed vs. model line profiles for Models A and B. As in the case of the moment 0 and P–V images and data cube renderings presented in Fig. 10 and Fig. 11, the model line profiles for the two models (shown in cyan in Fig. 12) are nearly indistinguishable. This Figure demonstrates that, in both cases, the simple 2-ring model described here can well reproduce the observed width and double-peaked profile of the bright line core, which is dominated by Ring 1. Both models also well reproduce the blueshifted “satellite peak” at $\sim 50 \text{ km s}^{-1}$ generated by Ring 2. However, the model fails to reproduce the detailed shapes of the line wings and the redshifted satellite peak at $\sim 0 \text{ km s}^{-1}$; the latter mismatch can be attributed to the patchy/knotty nature of the rearward (redshifted) side of Ring 2 (see Fig. 4, bottom frames).

³ <https://glueviz.org/>

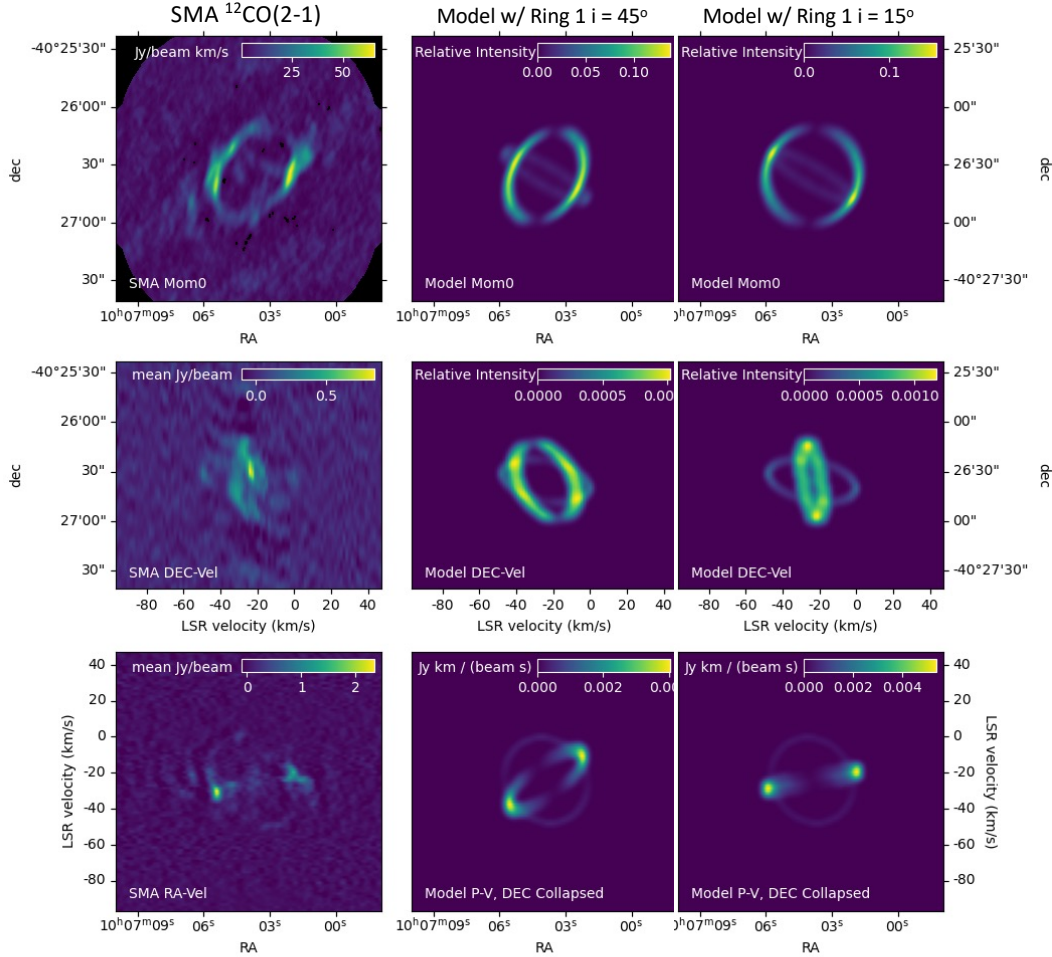


Figure 9. *Left panels:* The three views of the SMA $^{12}\text{CO}(2-1)$ data cube presented in Fig. 5. Top to bottom: velocity-integrated (moment 0) image; RA-collapsed P-V image; decl.-collapsed P-V image. *Middle panels:* the corresponding views of the simple geometrical model of CO emission for the case of two circular rings with identical radii and expansion velocities and inclinations of 45° for Ring 1 and 78° for Ring 2. *Right panels:* the corresponding views of the same model, but with the inclination set to 15° for Ring 1.

REFERENCES

- Bachiller, R., Forveille, T., Huggins, P. J., & Cox, P. 1997, *A&A*, 324, 1123
- Bisbas, T. G., Papadopoulos, P. P., & Viti, S. 2015, *ApJ*, 803, 37, doi: [10.1088/0004-637X/803/1/37](https://doi.org/10.1088/0004-637X/803/1/37)
- Bolatto, A. D., Wolfire, M., & Leroy, A. K. 2013, *ARA&A*, 51, 207, doi: [10.1146/annurev-astro-082812-140944](https://doi.org/10.1146/annurev-astro-082812-140944)
- Ciardullo, R., Bond, H. E., Sipior, M. S., et al. 1999, *AJ*, 118, 488, doi: [10.1086/300940](https://doi.org/10.1086/300940)
- De Marco, O. 2009, *PASP*, 121, 316
- De Marco, O., Akashi, M., Akras, S., et al. 2022, *Nature Astronomy*, 6, 1421, doi: [10.1038/s41550-022-01845-2](https://doi.org/10.1038/s41550-022-01845-2)
- Huggins, P. J., Bachiller, R., Cox, P., & Forveille, T. 1996, *A&A*, 315, 284
- Huggins, P. J., Bachiller, R., Planesas, P., Forveille, T., & Cox, P. 2005, *ApJS*, 160, 272, doi: [10.1086/432668](https://doi.org/10.1086/432668)
- Jones, D., & Boffin, H. M. J. 2017, *Nature Astronomy*, 1, 0117, doi: [10.1038/s41550-017-0117](https://doi.org/10.1038/s41550-017-0117)
- Karakas, A. I., & Lugaro, M. 2016, *ApJ*, 825, 26, doi: [10.3847/0004-637X/825/1/26](https://doi.org/10.3847/0004-637X/825/1/26)
- Kastner, J. H., Gatley, I., Merrill, K. M., Probst, R., & Weintraub, D. 1994, *ApJ*, 421, 600, doi: [10.1086/173675](https://doi.org/10.1086/173675)
- Kastner, J. H., Moraga Baez, P., Balick, B., et al. 2022, *ApJ*, 927, 100, doi: [10.3847/1538-4357/ac51cd](https://doi.org/10.3847/1538-4357/ac51cd)
- Kastner, J. H., Weintraub, D. A., Gatley, I., Merrill, K. M., & Probst, R. G. 1996, *ApJ*, 462, 777

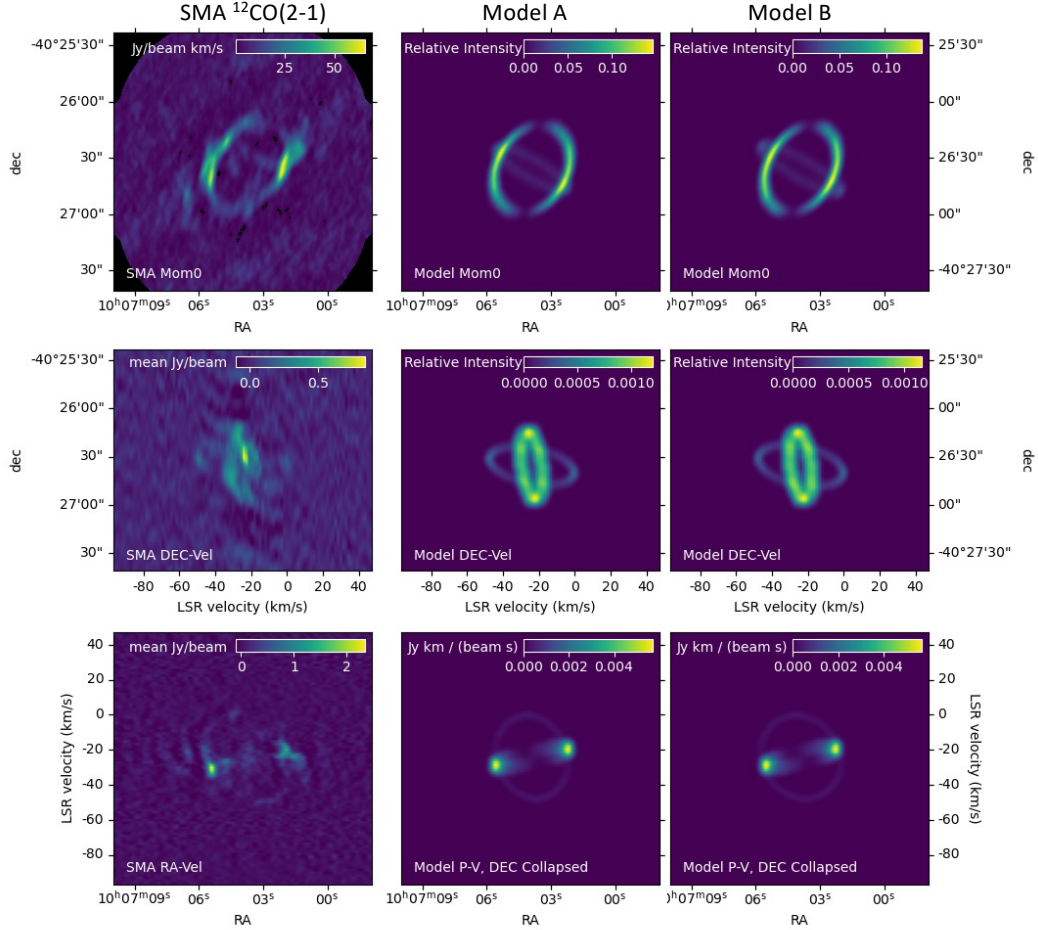


Figure 10. As in Fig. 9, for two revised models that attempt to more accurately reproduce Ring 1’s morphology in all three “collapsed” SMA data cube renderings (again shown in the *left panels*). *Middle panels:* The corresponding views of Model A, the simple geometrical model of CO emission for the case of an elliptical Ring 1 that has major/minor axis ratio 1.25 and is viewed at an inclination of 20° . *Right panels:* The corresponding views of Model B, the model for which Ring 1 is viewed at an inclination of 45° , as in the center column panels of Fig. 9, but its expansion velocity is reduced to 10 km s^{-1} ($2.5\times$ smaller than that of Ring 2), such that its dynamical age is 9250 yr ($2.5\times$ larger than that of Ring 2).

Kastner, J. H., Zijlstra, A., Balick, B., & Sahai, R. 2018, in *Astronomical Society of the Pacific Conference Series*, Vol. 517, *Science with a Next Generation Very Large Array*, ed. E. Murphy, 395

Monreal-Ibero, A., & Walsh, J. R. 2020, *A&A*, 634, A47, doi: [10.1051/0004-6361/201936845](https://doi.org/10.1051/0004-6361/201936845)

Monteiro, H., Morisset, C., Gruenwald, R., & Viegas, S. M. 2000, *ApJ*, 537, 853, doi: [10.1086/309058](https://doi.org/10.1086/309058)

Moraga Baez, P., Kastner, J. H., Bublitz, J., et al. 2023, in *American Astronomical Society Meeting Abstracts*, Vol. 55, *American Astronomical Society Meeting Abstracts*, 468.02

Rechy-García, J. S., Guerrero, M. A., Duarte Puertas, S., et al. 2020, *MNRAS*, 492, 1957, doi: [10.1093/mnras/stz3326](https://doi.org/10.1093/mnras/stz3326)

Sahai, R., Bujarrabal, V., Quintana-Lacaci, G., et al. 2023, *ApJ*, 943, 110, doi: [10.3847/1538-4357/aca7ba](https://doi.org/10.3847/1538-4357/aca7ba)

Sahai, R., & Trauger, J. T. 1998, *AJ*, 116, 1357

Sahai, R., Wootten, A., & Clegg, R. E. S. 1990, *A&A*, 234, L1

Sahai, R., Wootten, A., & Clegg, R. E. S. 1993, in *Planetary Nebulae*, ed. R. Weinberger & A. Acker, Vol. 155, 229

Santander-García, M., Bujarrabal, V., Alcolea, J., et al. 2017, *A&A*, 597, A27, doi: [10.1051/0004-6361/201629288](https://doi.org/10.1051/0004-6361/201629288)

Storey, J. W. V. 1984, *MNRAS*, 206, 521, doi: [10.1093/mnras/206.3.521](https://doi.org/10.1093/mnras/206.3.521)

van der Tak, F. F. S., Black, J. H., Schöier, F. L., Jansen, D. J., & van Dishoeck, E. F. 2007, *A&A*, 468, 627, doi: [10.1051/0004-6361:20066820](https://doi.org/10.1051/0004-6361:20066820)

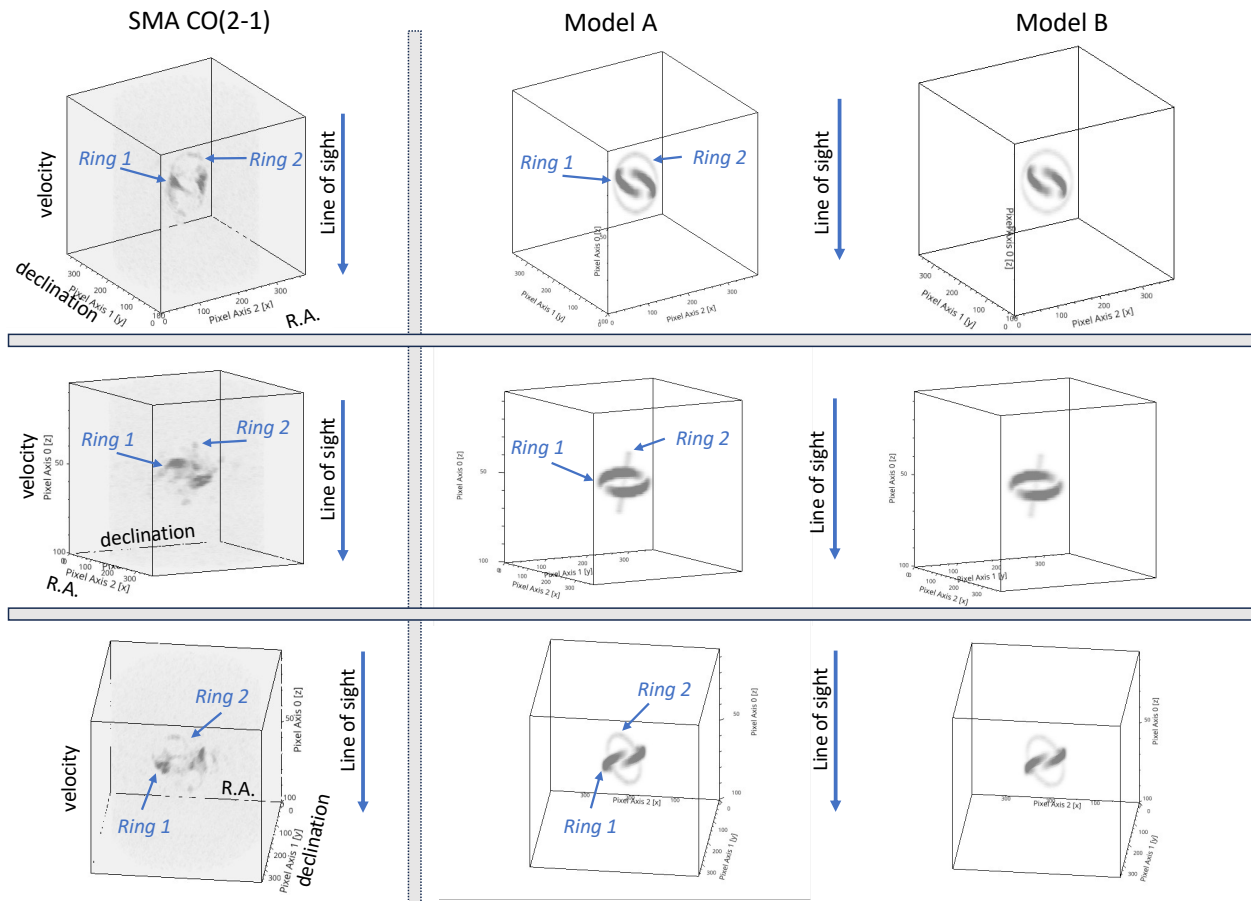


Figure 11. *Left panels:* Three example volume renderings of the SMA $^{12}\text{CO}(2-1)$ data cube, with RA, declination, and velocity as the x -axis, y -axis, and z -axis (respectively). The dimensions of the cube are $\sim 180''$ along the RA, dec (x, y) axes and -96 km s^{-1} to $+46 \text{ km s}^{-1}$ along the velocity (z) axis. *Middle panels:* The corresponding views of Model A. *Right panels:* The corresponding views of Model B.

Webster, B. L., Payne, P. W., Storey, J. W. V., & Dopita,

M. A. 1988, MNRAS, 235, 533,

doi: [10.1093/mnras/235.2.533](https://doi.org/10.1093/mnras/235.2.533)

Yu, M., Evans, Neal J., I., Dodson-Robinson, S. E., Willacy, K., & Turner, N. J. 2017, ApJ, 841, 39, doi: [10.3847/1538-4357/aa6e4c](https://doi.org/10.3847/1538-4357/aa6e4c)

Zuckerman, B., & Gatley, I. 1988, ApJ, 324, 501

Zuckerman, B., Kastner, J. H., Balick, B., & Gatley, I. 1990, ApJL, 356, L59

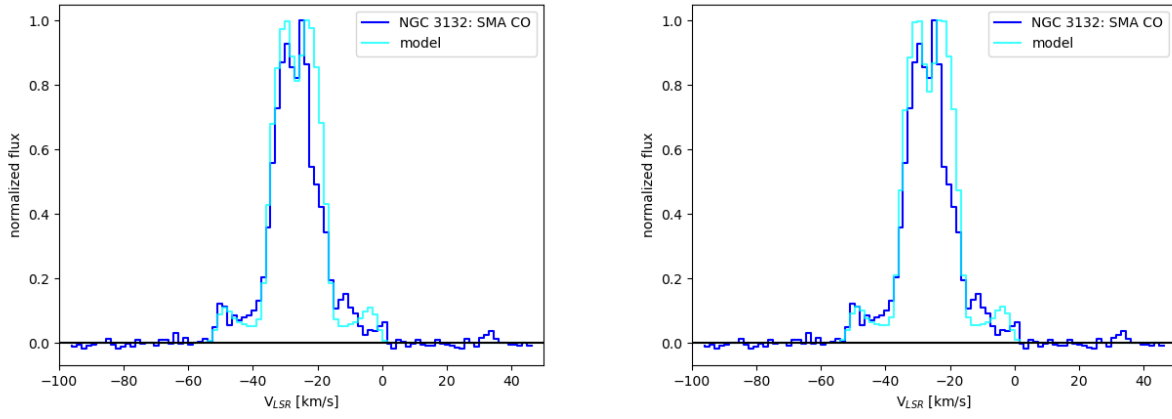


Figure 12. Comparisons of the spatially integrated SMA $^{12}\text{CO}(2-1)$ line profile of NGC 3132 (blue) with line profiles extracted from the data cubes constructed for Model A (left) and Model B (right), the simple geometrical models illustrated in Fig. 10 (cyan), using the same ($\sim 33''$ radius) extraction region.